

Article

Mixing Uncertainties in Low-Metallicity AGB Stars: The Impact on Stellar Structure and Nucleosynthesis

Umberto Battino ^{1,*}, Claudia Lederer-Woods ^{1,†}, Borbála Cseh ², Pavel Denissenkov ^{3,4,†} and Falk Herwig ^{3,4,†}

¹ School of Physics and Astronomy, University of Edinburgh, Edinburgh EH9 3FD, UK; Claudia.Lederer-Woods@ed.ac.uk

² Konkoly Observatory, Research Centre for Astronomy and Earth Sciences, Eötvös Loránd Research Network (ELKH), Konkoly Thege M. út 15-17, 1121 Budapest, Hungary; cseh.borbala@gmail.com

³ Department of Physics & Astronomy, University of Victoria, Victoria, BC V8P 5C2, Canada; pavel.denissenkov@gmail.com (P.D.); fherwig@uvic.ca (F.H.)

⁴ Joint Institute for Nuclear Astrophysics, Center for the Evolution of the Elements, Michigan State University, 640 South Shaw Lane, East Lansing, MI 48824, USA

* Correspondence: u.battino@ed.ac.uk

† The NuGrid Collaboration, <http://www.nugridstars.org>.

Abstract: The slow neutron-capture process (*s*-process) efficiency in low-mass AGB stars ($1.5 < M/M_{\odot} < 3$) critically depends on how mixing processes in stellar interiors are handled, which is still affected by considerable uncertainties. In this work, we compute the evolution and nucleosynthesis of low-mass AGB stars at low metallicities using the MESA stellar evolution code. The combined data set includes models with initial masses $M_{\text{ini}}/M_{\odot} = 2$ and 3 for initial metallicities $Z = 0.001$ and 0.002. The nucleosynthesis was calculated for all relevant isotopes by post-processing with the NuGrid mppnp code. Using these models, we show the impact of the uncertainties affecting the main mixing processes on heavy element nucleosynthesis, such as convection and mixing at convective boundaries. We finally compare our theoretical predictions with observed surface abundances on low-metallicity stars. We find that mixing at the interface between the He-intershell and the CO-core has a critical impact on the *s*-process at low metallicities, and its importance is comparable to convective boundary mixing processes under the convective envelope, which determine the formation and size of the ^{13}C -pocket. Additionally, our results indicate that models with very low to no mixing below the He-intershell during thermal pulses, and with a ^{13}C -pocket size of at least $\sim 3 \times 10^{-4} M_{\odot}$, are strongly favored in reproducing observations. Online access to complete yield data tables is also provided.

Keywords: evolved stars; stellar evolution; stellar interiors; stellar mixing; nucleosynthesis



Citation: Battino, U.; Lederer-Woods, C.; Cseh, B.; Denissenkov, P.; Herwig, F. Mixing Uncertainties in Low-Metallicity AGB Stars: The Impact on Stellar Structure and Nucleosynthesis. *Universe* **2021**, *7*, 25. <https://doi.org/10.3390/universe7020025>

Academic Editor: Sylvia Ekström
Received: 22 December 2020
Accepted: 22 January 2021
Published: 26 January 2021

Publisher's Note: MDPI stays neutral with regard to jurisdictional claims in published maps and institutional affiliations.



Copyright: © 2021 by the authors. Licensee MDPI, Basel, Switzerland. This article is an open access article distributed under the terms and conditions of the Creative Commons Attribution (CC BY) license (<https://creativecommons.org/licenses/by/4.0/>).

1. Introduction

Asymptotic giant branch (AGB) stars are important contributors to the chemical enrichment of our galaxy. In particular, low-mass AGB stars ($1.5 < M/M_{\odot} < 3$) are the main site of both the main and strong component of *s*-process ('slow' neutron-capture process [1–4]), i.e., the nucleosynthesis processes mainly responsible for around half of the neutron-capture element abundances between Zr and Bi in the solar system. The main component produces *s*-isotopes in the range of $90 < A \leq 204$, and takes place in low-mass AGB stars with around solar metallicity [5,6]. The strong component explains about half of the solar ^{208}Pb and is hosted by low-metallicity ($[\text{Fe}/\text{H}] \leq -1$), low-mass AGB stars (e.g., [7–9]). Throughout the present study, we will adopt the square-bracket notation to express elemental abundance ratios, which are defined as follows:

$$[X/Y] = \log((X_*/Y_*)/(X_{\odot}/Y_{\odot})). \quad (1)$$

The internal structure of AGB stars consists of an inert CO-core, surrounded by a He- and a H-shell where energy generation occurs alternatively. These two thin shells are located between the central CO-core and an extended H-rich convective envelope. Typically, the very-low-density convective envelope extends over a radius comparable to the Earth's orbit, while the central compact core contains about half to one solar-mass material inside an Earth-size volume. The convective nature of the external envelope is crucial for both the stellar structure and nucleosynthesis, as it represents the dominant energy transport mechanism and modifies surface composition with elements newly formed in the stellar interiors, impacting opacities and temperature gradients within the star. Additionally, convection generally induces convective boundary mixing (CBM) processes, for example, by inducing the propagation of internal gravity waves (IGWs [10]). Indeed, when enough He is accumulated in the H-shell by the H-shell burning further out, thin-shell instabilities and partial electronic degeneracy trigger a thermonuclear run-away caused by the unstable burning of He, called thermal-pulse (TP). The huge and sudden energy release makes the external envelope expand and cool, increasing its opacity. In turn, the higher opacity will increase the efficiency of convection within the envelope, which will then penetrate into the He-shell (an event called third dredge up, hereafter TDU), dredging up to the surface the elements freshly synthesized in the stellar interiors (including *s*-process elements). CBM processes during the TDU will deeply impact the nucleosynthesis during the AGB phase, allowing the diffusion of H-rich material into the C-rich He intershell. This will trigger formation of the so-called ^{13}C -pocket, which represents the main neutron source for *s*-process nucleosynthesis via the $^{13}\text{C}(\alpha, n)^{16}\text{O}$ reaction (see [3,11]). Over the last two decades, several studies attempted to consistently describe, in 1D stellar models, the CBM processes responsible for the formation of the ^{13}C -pocket. Initially, Ref. [12] proposed an exponentially decaying mixing-profile under the convective envelope during TDU. Subsequently, Ref. [13] proposed a rotationally induced CBM, and more recently, Ref. [14] computed for the first time full rotating AGB stellar models consistent with asteroseismology constraints, showing how rotation-induced mixing may have negligible effects on AGB heavy-element nucleosynthesis. An additional process that is potentially able to trigger mixing in stellar interiors is thermohaline, which was first introduced to the astrophysical community by [15] and revisited by [16]. Building on the results of [17,18], Ref. [19] determined the conditions under which thermohaline-driven instabilities and hence mixing may be expected. They concluded that the only two plausible scenarios where this may happen are RGB stars undergoing core He flashes and accreting white dwarfs, thus excluding thermohaline-mixing from playing a significant role in AGB stars.

Ref. [20] suggested that the formation of the ^{13}C -pocket can be induced by magnetic-buoyancy (based on the formalism by [21]). This last hypothesis was then tested by [22], who demonstrated that a wide range of isotopic ratios, measured in SiC presolar grains, can be simultaneously reproduced by adopting a single magnetic field configuration. However, there are some drawbacks affecting the robustness of this scenario, which warrant more work and discussion. Ref. [23] attempted to explain bipolar planetary nebulae morphologies through magnetic fields and found that initial magnetic fields quickly dissipate in the isolated star case and cannot be sustained for long enough, while a binary interaction can do so more robustly. Additionally, Ref. [24] showed that among H-rich DA white-dwarfs, the most numerous class of white dwarfs, only 4% show magnetic fields (see their Table 1).

Ref. [10] proposed a model based on IGWs induced by the convective motion in the envelope. A formalism to mimic in 1D the mixing induced by IGWs was developed and tested by [25], which was used by [26] to compute a grid of stellar evolution and full-nucleosynthesis models of low-mass AGB stars, with around solar metallicity and different initial masses. Furthermore, in this case, the majority of isotopic ratios from SiC presolar grains was well reproduced, except for $^{84}\text{Sr}/^{86}\text{Sr}$ and $^{137}\text{Ba}/^{138}\text{Ba}$ (the comparison with the measured $^{96}\text{Zr}/^{94}\text{Zr}$ was eventually much improved by adopting the new $^{22}\text{Ne}(\alpha, n)^{25}\text{Mg}$ reaction rate presented in [27], based on the recent measurement of [28]).

The main difference between models, adopting these different convective boundary mixing (CBM) formalisms, is the remarkable difference in the ^{13}C -pocket size and the relative abundances of ^{13}C and ^{14}N within the pocket, which directly impacts the total amount of s -process elements produced. Indeed, ^{14}N is a major neutron poison that competes with neutron captures on iron-group and heavier nuclei, reducing the s -process efficiency [29–32]. For example, the average ^{13}C -pocket size in [26] models was $\sim 10^{-4} M_{\odot}$, while [22] obtained a pocket size between 2 and $3 \times 10^{-3} M_{\odot}$. Moreover, Ref. [33] computed multi-D simulation of the He-flash in low-mass AGB star ($M = 2 M_{\odot}$ and $Z = 0.01$), showing how CBM is actually active under the intershell during TPs. Including this CBM under the He-intershell is indeed essential to reproduce the observed surface abundances of post-AGB H-deficient stars of the PG1159 class [34] and to match the highest observed [hs/l_s] (with hs and l_s being the average abundance of s -process elements at the second and first peak, respectively) on the surface of carbon stars. For these reasons it was included in all the models presented in [26]. On the other hand, this additional mixing was not included in [22].

The different methods to include mixing processes in 1D stellar models, reflected in the large range of s -process results presented in the literature, is indicative of the large stellar modeling uncertainties that are still affecting our understanding of AGB nucleosynthesis. Additionally, some of the CBM formalisms mentioned before were validated only for around solar metallicity models. The main reason for this is the large number of observations available for AGB stars with close to solar metallicities, which includes presolar grain measurements (e.g., [35]). However, even if only tested for near-solar metallicity models, these formalisms were then applied to the whole metallicity range, introducing more systematic uncertainties when investigating the s -process at low metallicities.

In this work, we compute the evolution and nucleosynthesis of low-mass AGB stars at low metallicities using the MESA stellar evolution code and the NuGrid mppnp code for the full nucleosynthesis [36]. The combined data set includes models with an initial mass of $M_{ZAMS}/M_{\odot} = 3$ for $Z = 0.001$. The main goal is to show the impact of the uncertainties affecting the main mixing processes, such as convection and mixing at convective boundaries, on heavy-element nucleosynthesis.

This work is organized as follows. In Section 2, we describe the stellar code and post-processing nucleosynthesis tools. In Section 3, the stellar models are presented, together with our nucleosynthesis results, before finally presenting our conclusions in Section 4.

2. Computational Methods

We used the stellar code MESA (revision 3709, [37]) to compute all the stellar models presented in this work. For the initial composition, we used the alpha-enhanced solar distribution based on [38], which implies a solar metallicity $Z_{\odot} = 0.018$. Additionally, in Table 1 we provide the initial carbon, nitrogen and oxygen (CNO) abundances adopted. The modeling assumptions are the same as in [39], except for CBM modeling, which is included the same way as in [25,26]. For the simulations, the MESA nuclear network *agb.net* is used, including 18 isotopes from protons to ^{22}Ne .

Table 1. Initial CNO abundances in mass fractions adopted for the stellar models presented in Tables 2 and 3.

Specie	Initial Abundance
Z = 0.001	
¹² C	1.25×10^{-4}
¹³ C	4.16×10^{-7}
¹⁴ N	1.06×10^{-5}
¹⁵ N	4.17×10^{-8}
¹⁶ O	7.41×10^{-4}
¹⁷ O	3.82×10^{-8}
¹⁸ O	2.17×10^{-7}
Z = 0.002	
¹² C	2.50×10^{-4}
¹³ C	8.32×10^{-7}
¹⁴ N	2.12×10^{-5}
¹⁵ N	8.35×10^{-8}
¹⁶ O	1.48×10^{-3}
¹⁷ O	7.63×10^{-8}
¹⁸ O	4.35×10^{-7}

Full nucleosynthesis simulations are obtained by using a post-processing code and the precalculated stellar structure. The post-processing code `mppnp` is described in detail in [36]. The stellar structure evolution data are computed and saved with MESA for all zones at all time steps, then used as inputs and processed with `mppnp`. This means that the stellar structure and the full nucleosynthesis are computed separately, hence requiring less computing time and resources. In order to maintain consistency between stellar and nucleosynthesis calculations, MESA and `mppnp` adopt the same nuclear reaction rates relevant for energy generation and, therefore, for the evolution of the star. The nuclear reaction rates adopted are the same as in [26]. Exceptions relevant for this work are the $^{22}\text{Ne}(\alpha, n)^{25}\text{Mg}$ and the $^{22}\text{Ne}(\alpha, \gamma)^{26}\text{Mg}$ reaction rates, for which we use [27].

3. Results

3.1. Description of the Stellar Models

Our stellar models are listed in Tables 2 and 3, giving details of our $M_{\text{ini}} = 3 M_{\odot}$ and $M_{\text{ini}} = 2 M_{\odot}$ models, respectively. Each model corresponds to a different setting of mixing processes inside the star. The same initial metallicity ($Z = 0.001$) is adopted for all models in Table 2. All models' names start with a 'm3z1m3'. The first 'm3' means that this is a $3 M_{\odot}$ model, and 'z1m3' is to be read as $Z = 1 \times 10^{-3}$, where the second 'm3' means 'minus three', referring to the exponent. The suffix abbreviations of the models' names indicate the internal mixing setting adopted. "–mlt" means that "mixing length theory" parameters different from other models have been tested, "–bigpoc" indicates that the model has a "bigger pocket of ^{13}C ", while "–nofTP" means that the CBM parameter f adopted under the intershell during a TP is zero. Tables 2 and 3 list key global features like core masses and lifetimes for all the models, which were all computed with the same stellar code and input physics of [39] (hereafter RI18), but with the CBM model of [25] during TDUs. The f_1 and f_2 parameters shown in both tables enter the CBM equation presented in [25] in order to mimic the mixing induced by internal gravity waves (IGWs).

Table 2. Main properties of our $3 M_{\odot}$ asymptotic giant branch (AGB) models: H-free core mass at the beginning and the end of the AGB phase (in solar masses), total lifetime, convective boundary mixing parameters during thermal pulses (TP), and third dredge-up events (TDU) and the adopted mixing-length parameter α are given. Core masses, total lifetimes, and mixing parameters in RI18 for models with the same mass/metallicity combinations are also presented. MLT—mixing-length theory.

Name	H-Free M_{ini}	H-Free M_{end}	τ_{tot} (years)	f_1 TDU	f_2 TDU	f_1 TP	α_{MLT}
m3z1m3	0.826	0.825	2.97×10^8	0.014	0.27	0.008	1.73
m3z2m3-mlt	0.849	0.848	3.01×10^8	0.014	0.27	0.008	1.55
m3z1m3-nofTP	0.826	0.835	2.97×10^8	0.014	0.27	-	1.73
m3z1m3-bigpoc	0.826	0.832	2.97×10^8	0.014	0.50	-	1.73
RI18	0.821	0.824	2.99×10^8	0.126	-	0.008	1.73

Table 3. Same as in Table 2, but for our $2 M_{\odot}$ AGB models. m2z1m3-bigpoc and m2z2m3-bigpoc have an initial metallicity of $Z = 0.001$ and $Z = 0.002$, respectively.

Name	H-Free M_{ini}	H-Free M_{end}	τ_{tot} [years]	f_1 TDU	f_2 TDU	f_1 TP	α_{MLT}
m2z1m3-bigpoc	0.591	0.682	8.53×10^8	0.014	0.50	-	1.73
m2z2m3-bigpoc	0.558	0.637	9.27×10^8	0.014	0.50	-	1.73

For a distance from the Schwarzschild boundary $dr < dr_2$, the diffusion coefficient profile is given by the exponentially-decaying diffusion mixing of [40]:

$$D(dr) = D_0 \times \exp(-2dr/(f_1 \times H_{p0})), \quad (2)$$

where dr is the geometric distance to the convective boundary. The term $f_1 \times H_{p0}$ identifies the scale height of the CBM regime. The values D_0 and H_{p0} are, respectively, the diffusion coefficient D and the pressure scale height at the convective boundary. A second, slower-decreasing mixing coefficient is included in the same way as in [25], in order to also consider the IGW contribution discussed by [10]. IGWs are the dominating CBM mechanism at a distance dr_2 from the Schwarzschild boundary, when the mixing coefficient defined in Equation (2) falls below a value D_2 defined as

$$D_2 = D_0 \times \exp(-2dr_2/(f_1 \times H_{p0})) \quad (3)$$

with length scale $f_2 \times H_{p0}$, which is adopted for distances $dr > dr_2$. Therefore, for $dr > dr_2$:

$$D(dr) = D_2 \times \exp(-2(dr - dr_2)/(f_2 \times H_{p0})), \quad (4)$$

$$= D_0 \times \exp(-2dr_2/(f_1 \times H_{p0})) \times \exp(-2(dr - dr_2)/(f_2 \times H_{p0})). \quad (5)$$

In our models, we adopt the same D_2 value as calibrated and adopted in [26], i.e., $D_2 = 4.3 \times 10^{11} \text{ cm}^2 \text{ s}^{-1}$.

We also included the $M_{ini} = 3 M_{\odot}$, $Z = 0.001$ model from RI18 in Table 2 as a reference. Notice that the full nucleosynthesis of the RI18 model has been recomputed, adopting the newest $^{22}\text{Ne}(\alpha, n)^{25}\text{Mg}$ and $^{22}\text{Ne}(\alpha, \gamma)^{26}\text{Mg}$ nuclear reaction rates from [27]. The grid of models presented explores the impact of different combinations of mixing parameters. In particular, one of the biggest uncertainties in 1D AGB models is the treatment of convection, which would require 3D modeling [41–43]. The most adopted treatment in 1D stellar evolution relies on mixing-length theory (MLT [44,45]). The free mixing-length parameter α_{MLT} specifies the mean free path (i.e., the mixing-length) of a convective blob in units of the pressure scale height, and is usually calibrated on the Sun. Ref. [46] claimed that a mixing-length dependent on metallicity is required to match the surface temperatures of red giants in the APOKASC catalog [47], reporting a decreasing mixing-length when

decreasing metallicity of about 0.16 per metallicity dex. Based on [46] results, m3z1m3-mlt adopts a lower α_{MLT} parameter compared to the one adopted for solar metallicity models in [26], while all other models in Table 2 keep the solar-calibrated value. Indeed, a remarkable impact on the initial H-free core mass (which is then reflected on the final core mass) is visible when considering model m3z1m3-mlt. This is due to the fact that reducing the α_{MLT} directly impacts convection efficiency in the star, in particular, the second-dredge up, which is what stops the H-free core growth after the end of core He-burning. On the other hand, Ref. [48] derived a mixing-length parameter from their 3D simulations of the external part of the AGB envelope convection. They found $\alpha_{MLT} = 2.6$, larger than our solar-calibrated value, in contrast with the value for m3z1m3-mlt. Ref. [48] results point to a strong evolutionary phase dependence of the mixing-length, which is not included in the simpler metallicity-dependence relation derived by [46].

Another relevant impact, visible from Table 2, comes from the treatment of CBM under the He-intershell during TPs. Both m3z1m3-nofTP and m3z1m3-bigpoc do not include this CBM. As a consequence, they both show a higher final H-free core mass compared to m3z1m3, where CBM during TPs is included. The reason is shown in Figure 1. The upper panel shows the Kippenhahn diagram of m3z1m3-nofTP zoomed in the He-intershell. The lower panel presents the same kind of diagram, but it shows the structure evolution of m3z1m3. When a He-flash occurs in the intershell, it develops a pulse-driven convective zone (PDCZ) mixing the whole intershell, which is then followed by a TDU event, where the hydrogen convective envelope penetrates into the H-free core. The major difference between the two stellar structures is the lower reduction of the H-free core size immediately after a TDU event, which is the main cause of the difference in the final core size, in particular, after the first five TDUs. This is due to the lower He-flash luminosity of m3z1m3-nofTP compared to m3z1m3, as shown in Figure 2. A lower luminosity of the He-flashes leads to a smaller expansion of the convective envelope, and consequently, it will cool down less. This will cap the opacity increase in the envelope, limiting the increase of convection efficiency in the envelope. This will directly impact the TDU penetration into the He-intershell, which is visibly reduced in m3z1m3-nofTP compared to m3z1m3. The origin of this difference in the luminosity of He-flashes lies in the different He abundance in the intershell, as shown in Figure 3, which is up to 40% less abundant in m3z1m3. This is a direct consequence of the different treatment of CBM under the PDCZ, since through CBM, C-rich material can be dredged-up into the intershell from the core, decreasing the He mass-fraction. In turn, a lower abundance of He causes the higher temperature necessary to trigger the He-flash.

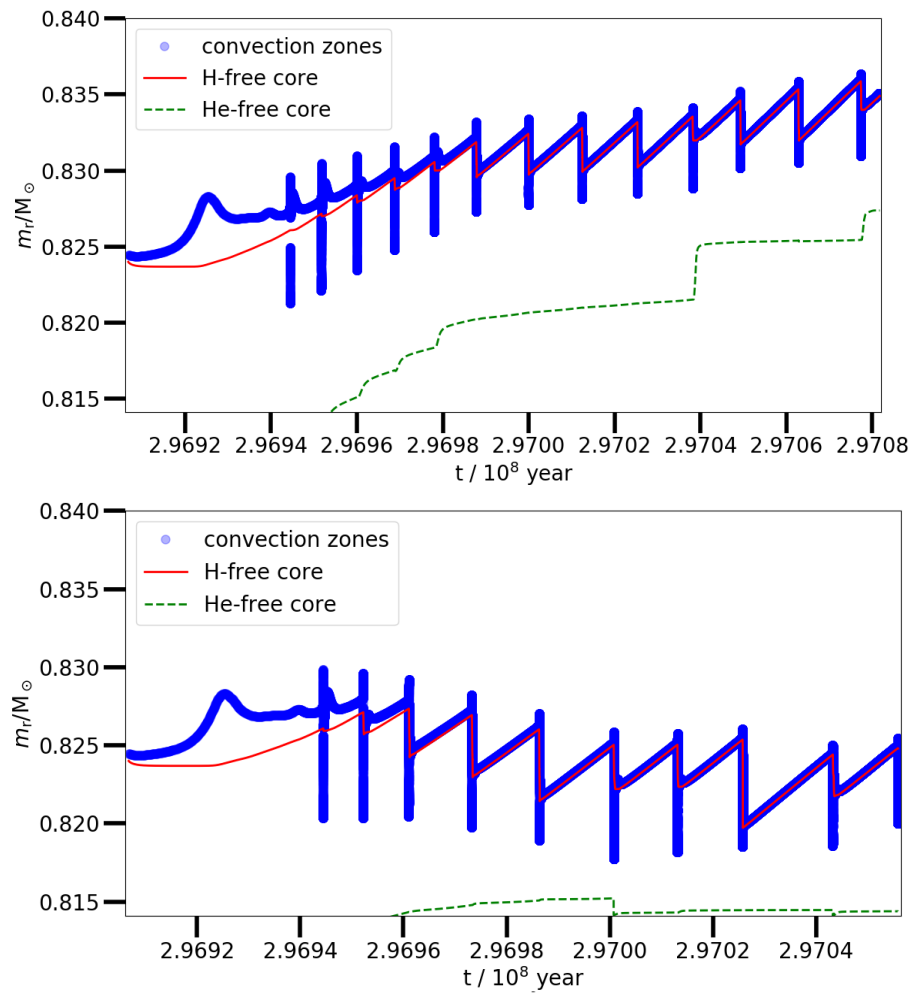


Figure 1. Upper panel: Kippenhahn diagram of m3z1m3-nofTP zoomed in the He-intershell. Lower panel: same as in the upper panels, but for m3z1m3.

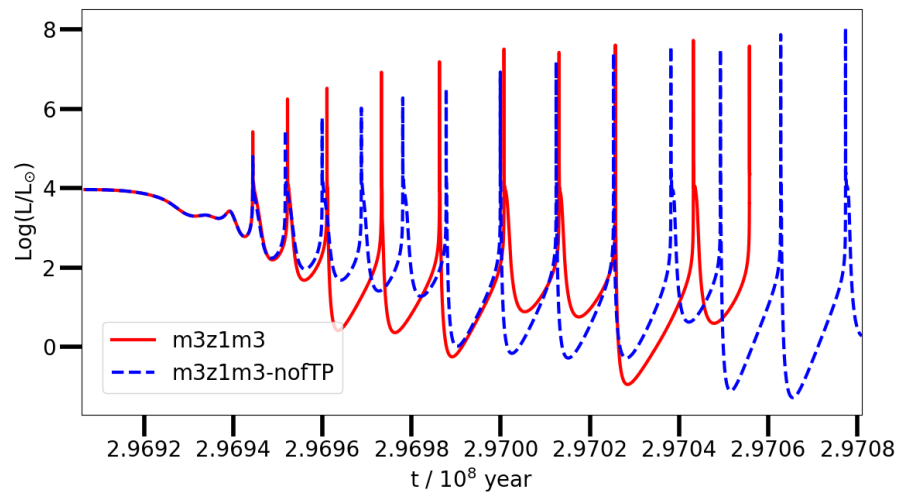


Figure 2. Evolution of He-burning luminosities over time in both m3z1m3 and m3z1m3-nofTP.

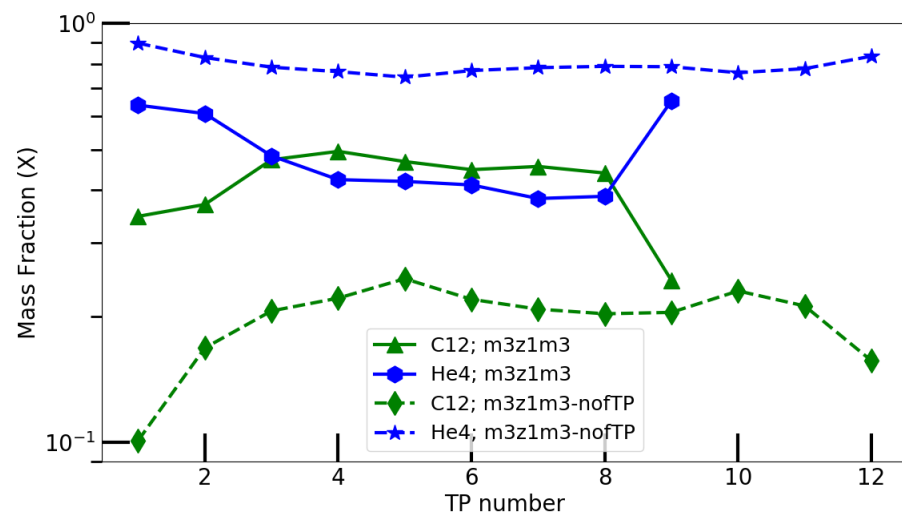


Figure 3. Evolution of ^{12}C and ^4He abundances in the intershell of m3z1m3 and m3z1m3-nofTP.

The slightly lower core mass of m3z1m3-bigpoc, compared to m3z1m3-nofTP, is due to the higher CBM efficiency under the convective envelope during TDUs, which also has a strong direct impact on heavy element nucleosynthesis (see next chapter). CBM parameters in m3z1m3-nofTP during TDUs are the same ones adopted in [26], guided by the internal gravity waves mixing profile in solar metallicity AGB stars obtained by [10]. However, as already discussed, this may not apply to the different structure of low-Z AGB stars. Hence, we explore the effects of a stronger CBM under the convective envelope. Indeed, this causes a deeper diffusion of hydrogen from the envelope, forming a bigger ^{13}C -pocket, as shown in Figure 4. In particular, the average ^{13}C -pocket size in m3z1m3-bigpoc is between 3 and $4 \times 10^{-4} M_{\odot}$, about a factor of three larger than the pocket size formed in m3z1m3-nofTP.

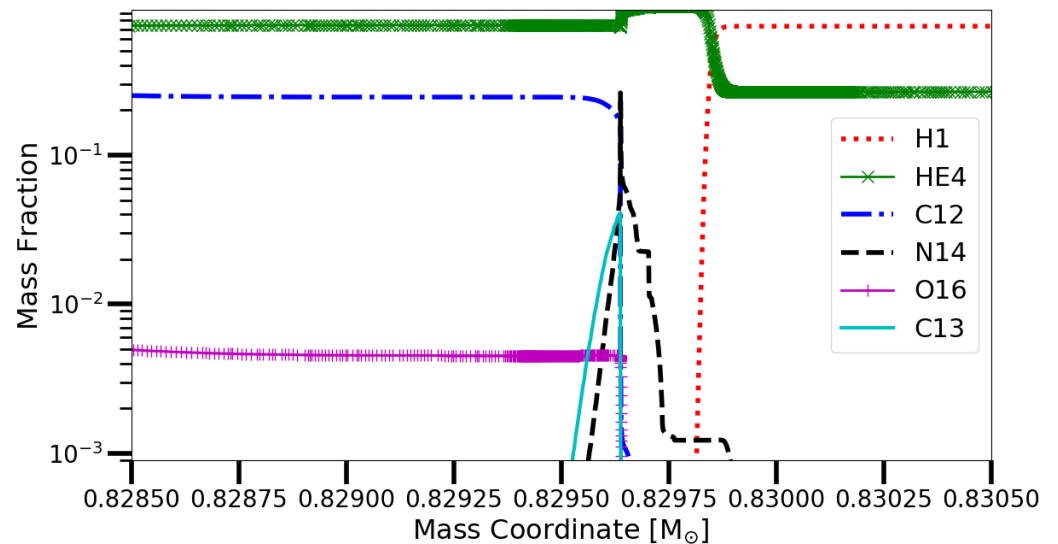


Figure 4. Cont.

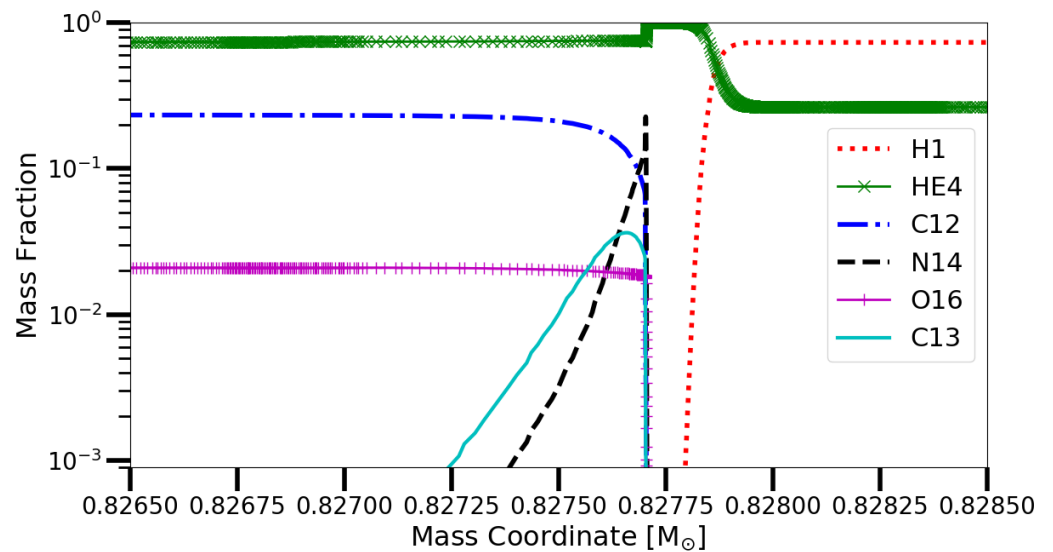


Figure 4. Upper panel: ^{13}C -pocket at the end of the oxygen-rich phase from m3z1m3. Lower panel: ^{13}C -pocket at the end of the oxygen-rich phase from m3z1m3-bigpoc. The comparison shows a much larger pocket formed by m3z1m3-bigpoc compared to m3z1m3 (about a factor of three) as a consequence of the slower decay of the mixing coefficient adopted for this model (see Table 2 for the mixing parameters adopted).

3.2. Postprocessing Nucleosynthesis Calculations

The *s*-process nucleosynthesis in low-mass AGB stars heavily depends on internal mixing processes. The resulting heavy element production of all the models presented in this work is shown in Figure 5. In the upper panel, RI18 exhibits the lowest *s*-process production, globally between a factor of two and three lower compared to m3z1m3, whose only difference from RI18 is a more efficient CBM under the convective envelope, which produces a ^{13}C -pocket about three times larger. The same difference is visible when comparing m3z1m3 with m31m3-bigpoc in the lower panel, since in this case, the typical ^{13}C -pocket also differs by a factor of three between the two models. Surface abundances of the Ba star HD 123396 [49] and CEMP-*s* star HD 26 [50] for two first-peak elements (Y and Zr), two second-peak elements (Ce and Nd), and Pb are also plotted for comparison. The two Pb abundances are only from HD 26, with the higher one being determined including non-LTE correction. m3z1m3-bigpoc is the only model consistent with first, second, and third *s*-process peak elements at the same time. Unfortunately, Pb abundances are not available for most of the sample stars we selected, and the determination of Pb abundances has some difficulties, often introducing big uncertainties [51–53]. Considering elements lighter than first-peak ones, m3z1m3 shows high enrichment, as shown in more detail in Figure 6, zoomed in the $30 < A < 41$ region. The [Rb/Sr] ratio is visibly higher in m3z1m3 compared to both m3z1m3-nofTP and m3z1m3-bigpoc. In particular, we recall that the only difference between m3z1m3 and m3z1m3-nofTP is the inclusion of CBM processes under the He-intershell in m3z1m3, while they are not considered in m3z1m3-nofTP. As we already discussed, this causes more luminous and hotter TPs, which eventually results in opening both the ^{85}Kr and ^{86}Rb branching points, efficiently producing both the neutron magic ^{86}Kr and ^{87}Rb isotopes. This high enrichment in Kr and Rb during the TP is then converted into Sr, Y, and Zr by neutron captures during the radiative burning of the ^{13}C -pocket. It is worth noticing that it is harder for the *s*-process nucleosynthesis flux to go past the first peak passing through ^{86}Kr and ^{87}Rb , compared to the lower neutron-density case where the two branching points are less open and ^{86}Sr is produced. Indeed, in high-neutron density conditions, caused by an efficient $^{22}\text{Ne}(\alpha, n)^{25}\text{Mg}$ in hot TPs, the neutron-capture chain will need to take place on four to five neutron magic nuclei, compared to only three in the case of colder TPs. This will cause substantial over-production of first-peak elements, and therefore, a lower [Ce/Y] in m3z1m3 compared to both m3z1m3-nofTP and

m3z1m3-bigpoc. This last aspect is confirmed by Figure 7. The [Ce/Y] ratio was used by Cseh et al. [49] as a representative of the [hs/ls] ratio. These elements were chosen based on the reliability and accuracy of the determined abundances of the sample Ba stars in their study, since Ba abundances were not available and [La/Fe] showed unexpectedly high values for some of the sample stars. [hs/Y] and [hs/Zr] show very similar ratios; here, we use [Ce/Y] to match their choice. The colored area between the two vertical dashed lines in Figure 7 indicates the range within which 80% of our low-Z AGB abundance observations are found. Despite the fact m3z1m3-nofTP is not able to reproduce the full [Ce/Y] range, it is still the best performing model among those presented in the figure when compared to observations. This suggests that models with no CBM under the He-intershell are largely favored, as this is apparently an essential condition to reproduce the observed high [Ce/Y] on low-Z AGB surfaces.

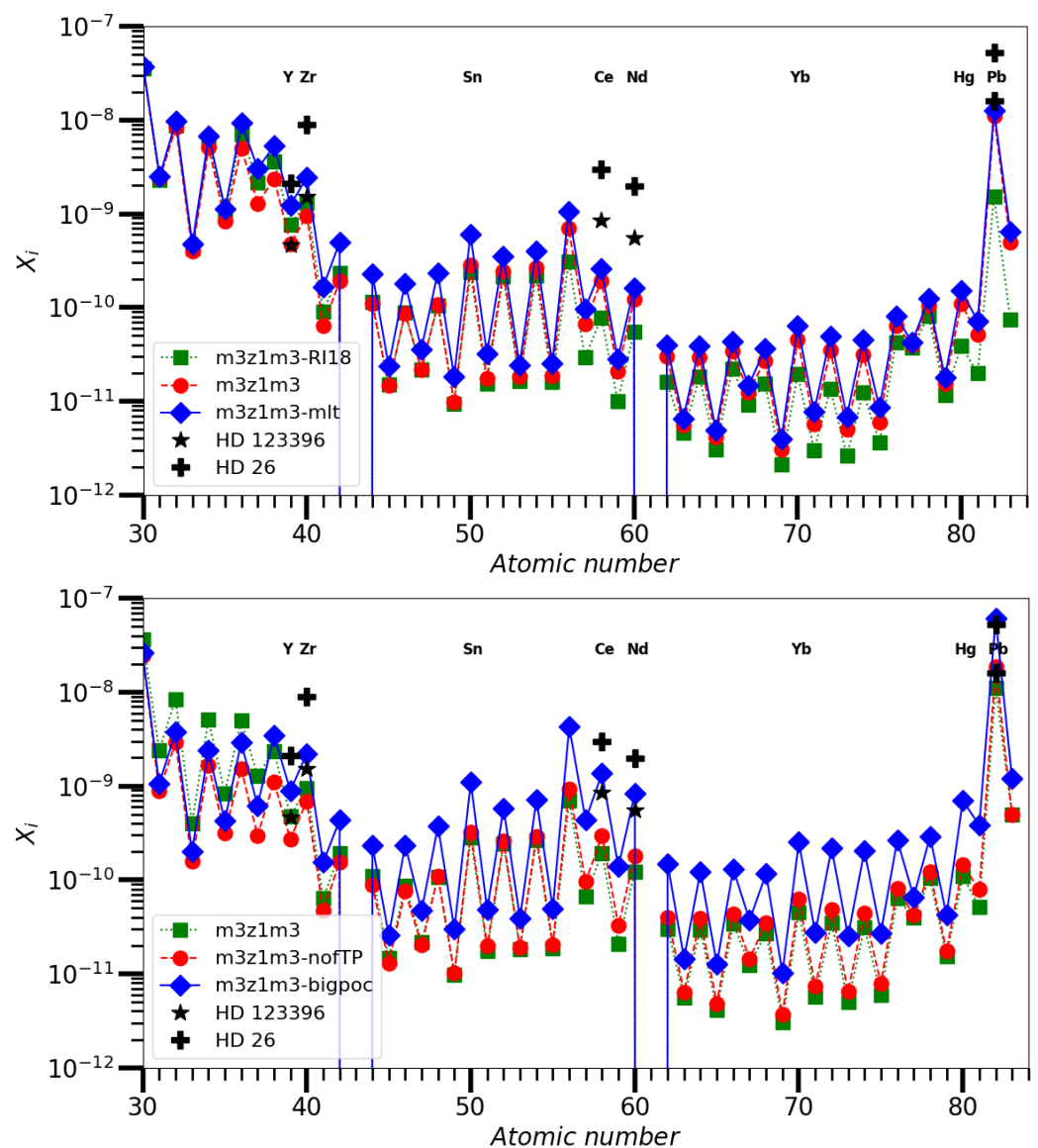


Figure 5. Upper panel: Heavy-element mass fractions of m3z1m3, m3z1m3-mlt, and the model from RI18 with the same mass and metallicity. Surface abundances of the Ba star HD 123396 [49] and CEMP-s star HD 26 [50] for two first-peak (Y and Zr) and second-peak elements (Ce and Nd); Pb are also plotted for comparison. The two Pb abundances are only from HD 26, with the higher one being determined including non-LTE correction. Lower panel: Same as in the upper panel, but for m3z1m3, m3z1m3-nofTP, and m3z1m3-bigpoc.

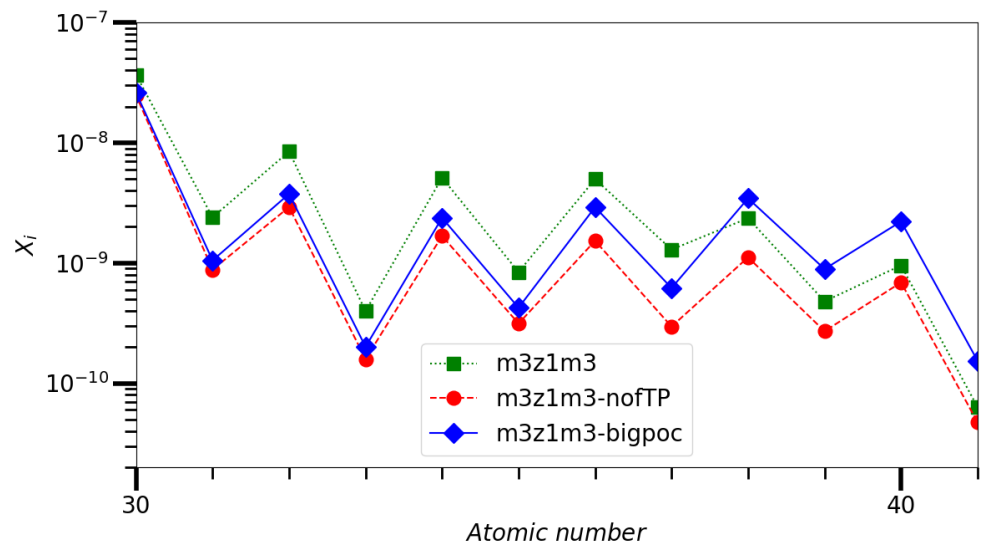


Figure 6. Heavy-element mass fractions of m3z1m3, m3z1m3-nofTP, and m3z1m3-bigpoc, zoomed in the $30 < A < 41$ region. The [Rb/Sr] ratio is visibly higher in m3z1m3 compared to both m3z1m3-nofTP and m3z1m3-bigpoc.

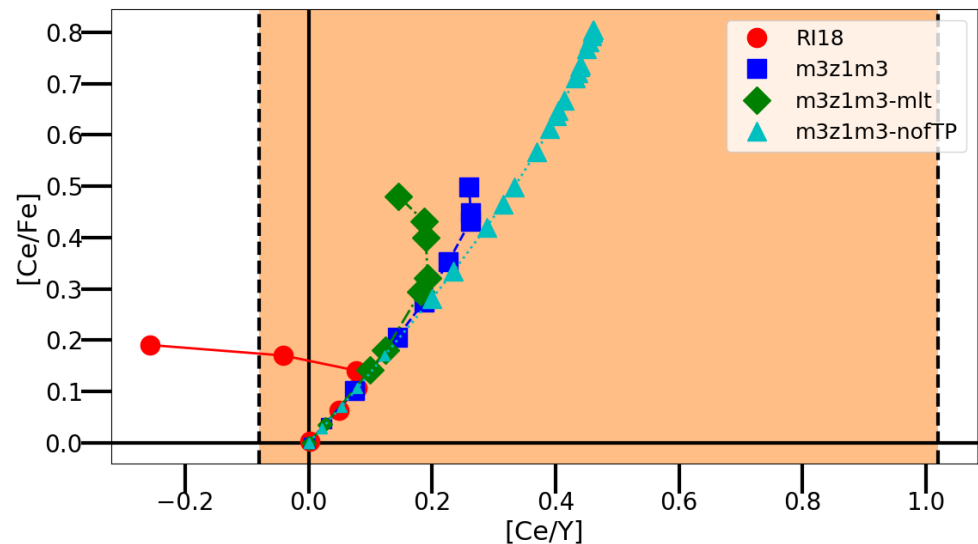


Figure 7. Comparison of [Ce/Fe] vs. [Ce/Y] results from the whole evolution of m3z1m3, m3z1m3-mlt, m3z1m3-nofTP, and the $3 M_{\odot}$ model from RI18. The two vertical dashed lines indicate the range within which 80% of low-Z AGB abundance observations are found.

On the other hand, Ref. [33] performed multi-D simulations of the TP in a $Z = 0.01$ AGB star. They found that mixing across convective boundaries is significant for He-shell flash convection. Guided by these findings, Refs. [25,26] implemented a consistent CBM under the He-intershell during TPs in their around solar-metallicity models. However, the $Z = 0.001$ models presented here are remarkably different from their $Z = 0.01$ counterparts with the same mass. For example, m3z1m3 from this work has an H-free core mass about $0.15 M_{\odot}$ larger than m3z1m2 ($M = 3 M_{\odot}$, $Z = 0.01$) in [26]. This means that the conditions found in m3z1m3 are probably significantly different from those explored by [33], questioning the validity of their results in low-Z AGBs. In particular, a significantly massive core is also more compact, hence, possibly inhibiting CBM processes at the interface with the He-intershell.

In Figure 8, we show again our predicted [Ce/Fe] vs. [Ce/Y], but including m3z1m3-bigpoc, m2z1m3-bigpoc, m2z2m3-bigpoc, and the observed abundances from different objects enriched with s-process elements from AGB stars: 10 post-AGBs [54,55], CEMP-s [50]

and Ba stars [49,56–58]. Names, references and [Fe/H] for each star are given in Table 4. CEMP-s and Ba stars are members of a binary system, in which the accreted material from the former AGB companion polluted the now-observed star. Thus, these stars retain the abundance pattern of their AGB companion, and are appropriate for comparison with AGB nucleosynthesis models. The straight line across the observational data is a linear regression showing the general trend of observed abundances. Comparing m3z1m3-bigpoc and m3z1m3-nofTP, we conclude that a very low to no CBM under the He-intershell is a necessary yet insufficient condition to reproduce the bulk of the observed s-process values. Indeed, a ^{13}C -pocket as large as in m3z1m3-bigpoc, i.e., typically $3 \times 10^{-4} M_{\odot}$, is an additional essential condition to be in agreement with the observed abundances. Hence, any CBM process under the convective envelope during TDUs and included in stellar models should be efficient enough to produce a ^{13}C -pocket as large as at least $3 \times 10^{-4} M_{\odot}$. Additionally, m3z1m3-bigpoc is consistent with both models with the same mass and metallicity from the FRUITY database [59,60], which did not include CBM under the He-intershell and form a ^{13}C -pocket comparable in size to m3z1m3-bigpoc ones. Both FRUITY and [60] models are also shown in Figure 8.

Table 4. Overview of the observational sample: names, references, and [Fe/H] are given for each star.

Name	[Fe/H]	Reference
Ba stars		
HD 123396	−1.04	[49]
HD 130255	−1.11	[49]
BD+09 2384	−0.98	[49]
HD 10613	−0.82	[56]
HD 121447	−0.90	[58]
Post-AGB stars		
J050632	−1.22	[54]
J052043	−1.17	[54]
J053250	−1.22	[54]
IRAS 07134	−0.91	[55]
CEMP-s stars		
HD 26	−0.98	[50]

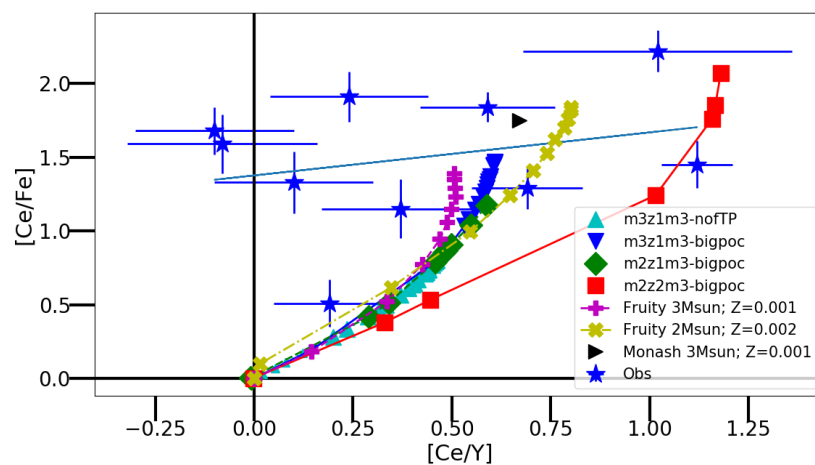


Figure 8. Comparison of [Ce/Fe] vs. [Ce/Y] results from the final surface abundances of m31m3-nofTP, m3z1m3-bigpoc, m2z1m3-bigpoc, and m2z2m3-bigpoc. Here, we also include results from the FRUITY database and the Monash group models as a comparison. Observed abundances from 10 post-AGB [55,61], CEMP-s [50], and Ba stars [49,56,58] are also included. The straight line across the observational data is a linear regression showing the general trend of observed abundances.

Finally, we notice how adding our $2 M_{\odot}$ models helps with covering the observed range of both $[\text{Ce}/\text{Fe}]$ and $[\text{Ce}/\text{Y}]$. As expected, the higher metallicity of m2z2m3-bigpoc causes less compact and a hotter interior, leading to less-efficient Rb production during TPs. As already discussed (e.g., Figure 6), this translates into lower first-peak element abundances, increasing the $[\text{Ce}/\text{Y}]$ ratio. In particular, m2z2m3-bigpoc successfully matches the two most-enriched *s*-process stars in the sample, with a surface $[\text{Ce}/\text{Y}] > 1$. This means that at least part of the observed spread in *s*-process efficiencies can be explained by a variation of mass and metallicity. Consistent with our models, the FRUITY $2 M_{\odot}$, $Z = 0.002$ model shows both a $[\text{Ce}/\text{Fe}]$ and $[\text{Ce}/\text{Y}]$ higher than its $3 M_{\odot}$, $Z = 0.001$ counterpart. On the other hand, several nuclear and stellar evolution uncertainties, such as those related to stellar binarity, can still have an impact. For instance, one could speculate that a mass transfer event from a massive AGB companion, which typically produces an envelope composition with $[\text{Ce}/\text{Y}] < 0$ (e.g., [39,62]), might be able to explain those stars with both high $[\text{Ce}/\text{Fe}]$ and $[\text{Ce}/\text{Y}]$ close to zero. We will explore this hypothesis in detail in a follow-up study (Battino et al. 2021b in preparation).

4. Conclusions

In this work, we computed the evolution and nucleosynthesis of low-mass AGB stars at low metallicities ($Z = 0.001$ and 0.002), testing the impact of the uncertainties affecting the main mixing processes, such as convection and mixing at convective boundaries, on heavy element nucleosynthesis.

We found that in order to be consistent with observed heavy-element abundances, AGB models should include no CBM under the He-intershell, though a CBM process under the convective envelope, efficient enough to form a large ^{13}C -pocket of at least $3 \times 10^{-4} M_{\odot}$, is required. In this way, our models show a final surface composition with $1.16 < [\text{Ce}/\text{Fe}] < 2.08$ and $0.61 < [\text{Ce}/\text{Y}] < 1.20$, consistent with the bulk of observations. We will verify in a forthcoming study if internal gravity waves are actually capable of producing such a ^{13}C -pocket in low- Z AGB stars.

Uncertainties related to the treatment of convection through parametric MLT impact the final $[\text{Ce}/\text{Y}]$ by about ± 0.1 dex. On one hand, this is minor compared to the role of CBM at convective boundaries, yet, enough to make future improvement of the handling of convection in 1D stellar models highly desirable, especially considering the visible impact on core masses.

Additionally, Pb abundances (third peak of the *s*-process) are important to understand the nucleosynthetic processes leading to the overabundance of this element in *s*-process enriched stars. Unfortunately, Pb abundances are not available for most of our sample stars and the determination of Pb abundances has some difficulties: the Pb I line at 4057.8 \AA , detectable in the optical wavelength, is often blended with CH and needs high-resolution, high signal-to-noise blue spectra for the derivation of the abundance. Additionally, the inclusion of non-LTE corrections is necessary to the most accurate comparison of the models with Pb and other elements [51–53]. Pb abundances from CEMP-*s* star HD 26 are indeed reproduced by our m3z1m3-bigpoc model, but larger statistical modeling is still prevented by the observational difficulties just mentioned.

Further uncertainties affecting the production of heavy elements, yet only briefly mentioned in this work, originate from nuclear physics and stellar binarity, which could in principle explain the spread in observed $[\text{Ce}/\text{Y}]$ values, in particular, the lowest ones. These additional sources of uncertainties will be investigated in detail in a forthcoming paper (Battino et al. 2021b in preparation).

Author Contributions: Conceptualization, U.B.; methodology, U.B.; software, U.B. and F.H.; validation, U.B., B.C., and C.L.-W.; formal analysis, U.B.; investigation, U.B.; resources, C.L.-W.; data curation, U.B. and B.C.; writing—original draft preparation, U.B.; writing—review and editing, C.L.-W., B.C., P.D., and F.H.; visualization, U.B.; supervision, C.L.-W.; project administration, U.B.; funding acquisition, C.L.-W. All authors have read and agreed to the published version of the manuscript.

Funding: This work received support from the Science and Technology Facilities Council UK (ST/M006085/1), and the European Research Council ERC-2015-STG Nr. 677497. This article is based upon work from the ChETEC COST Action (CA16117), supported by COST (European Cooperation in Science and Technology). B. Cs. acknowledges the support of the Hungarian National Research, Development and Innovation Office (NKFI), grant KH-18 130405.

Institutional Review Board Statement: Not applicable.

Informed Consent Statement: Not applicable.

Data Availability Statement: The data presented in this study are openly available in NuGRID repository, as specified at <https://nugrid.github.io/content/data>.

Acknowledgments: This research was enabled in part by support provided by WestGrid (www.westgrid.ca) and Compute Canada Calcul Canada (www.computecanada.ca). The computing facilities (in particular the Orcinus cluster) was mostly supported by the UBC Chemistry Department Team led by Mark Thachuk. NuGrid data is served by Canfar CADM and Globus (www.globus.org).

Conflicts of Interest: The authors declare no conflict of interest.

References

1. Cameron, A.G.W. Nuclear Reactions in Stars and Nucleogenesis. *Publ. Astron. Soc. Pac.* **1957**, *69*, 201. [[CrossRef](#)]
2. Burbidge, E.M.; Burbidge, G.R.; Fowler, W.A.; Hoyle, F. Synthesis of the Elements in Stars. *Rev. Mod. Phys.* **1957**, *29*, 547–650. [[CrossRef](#)]
3. Gallino, R.; Arlandini, C.; Busso, M.; Lugaro, M.; Travaglio, C.; Straniero, O.; Chieffi, A.; Limongi, M. Evolution and Nucleosynthesis in Low-Mass Asymptotic Giant Branch Stars. II. Neutron Capture and the s-Process. *Astrophys. J.* **1998**, *497*, 388. [[CrossRef](#)]
4. Käppeler, F.; Gallino, R.; Bisterzo, S.; Aoki, W. The s process: Nuclear physics, stellar models, and observations. *Rev. Mod. Phys.* **2011**, *83*, 157–194. [[CrossRef](#)]
5. Ulrich, R.K. The s-Process in Stars. In *Explosive Nucleosynthesis*; Schramm, D.N., Arnett, W.D., Eds.; University of Texas Press: Austin, TX, USA; London, UK, 1973; p. 139.
6. Iben, I., Jr.; Renzini, A. Asymptotic giant branch evolution and beyond. *Annu. Rev. Astron. Astrophys.* **1983**, *21*, 271–342. [[CrossRef](#)]
7. Clayton, D.D.; Rassbach, M.E. Termination of the s-PROCESS. *Astrophys. J.* **1967**, *148*, 69. [[CrossRef](#)]
8. Travaglio, C.; Gallino, R.; Busso, M.; Gratton, R. Lead: Asymptotic Giant Branch Production and Galactic Chemical Evolution. *Astrophys. J.* **2001**, *549*, 346–352. [[CrossRef](#)]
9. Bisterzo, S.; Gallino, R.; Käppeler, F.; Wiescher, M.; Imbriani, G.; Straniero, O.; Cristallo, S.; Görres, J.; deBoer, R.J. The branchings of the main s-process: Their sensitivity to α -induced reactions on ^{13}C and ^{22}Ne and to the uncertainties of the nuclear network. *Mon. Not. R. Astron. Soc.* **2015**, *449*, 506–527. [[CrossRef](#)]
10. Denissenkov, P.A.; Tout, C.A. Partial mixing and formation of the ^{13}C pocket by internal gravity waves in asymptotic giant branch stars. *Mon. Not. R. Astron. Soc.* **2003**, *340*, 722–732. [[CrossRef](#)]
11. Straniero, O.; Gallino, R.; Busso, M.; Chieffi, A.; Raiteri, C.M.; Limongi, M.; Salaris, M. Radiative C-13 burning in asymptotic giant branch stars and s-processing. *Astrophys. J.* **1995**, *440*, L85–L87. [[CrossRef](#)]
12. Herwig, F.; Blöcker, T.; Schönberner, D.; El Eid, M.F. Stellar evolution of low and intermediate-mass stars. IV. Hydrodynamically-based overshoot and nucleosynthesis in AGB stars. *Astron. Astrophys.* **1997**, *324*, L81–L84.
13. Langer, N.; Heger, A.; Wellstein, S.; Herwig, F. Mixing and nucleosynthesis in rotating AGB stars. *Astron. Astrophys.* **1999**, *346*, L37–L40.
14. Den Hartogh, J.W.; Hirschi, R.; Lugaro, M.; Doherty, C.L.; Battino, U.; Herwig, F.; Pignatari, M.; Eggenberger, P. The s process in rotating low-mass AGB stars. Nucleosynthesis calculations in models matching asteroseismic constraints. *Astron. Astrophys.* **2019**, *629*, A123. [[CrossRef](#)]
15. Ulrich, R.K. Thermohaline Convection in Stellar Interiors. *Astrophys. J.* **1972**, *172*, 165. [[CrossRef](#)]
16. Kippenhahn, R.; Ruschenplatt, G.; Thomas, H.C. The time scale of thermohaline mixing in stars. *Astron. Astrophys.* **1980**, *91*, 175–180.
17. Brown, J.M.; Garaud, P.; Stellmach, S. Chemical Transport and Spontaneous Layer Formation in Fingering Convection in Astrophysics. *Astrophys. J.* **2013**, *768*, 34. [[CrossRef](#)]
18. Traxler, A.; Stellmach, S.; Garaud, P.; Radko, T.; Brummell, N. Dynamics of fingering convection. Part 1 Small-scale fluxes and large-scale instabilities. *J. Fluid Mech.* **2011**, *677*, 530–553. [[CrossRef](#)]
19. Garaud, P.; Medrano, M.; Brown, J.M.; Mankovich, C.; Moore, K. Excitation of Gravity Waves by Fingering Convection, and the Formation of Compositional Staircases in Stellar Interiors. *Astrophys. J.* **2015**, *808*, 89. [[CrossRef](#)]
20. Trippella, O.; Busso, M.; Palmerini, S.; Maiorca, E.; Nucci, M.C. s-Processing in AGB Stars Revisited. II. Enhanced ^{13}C Production through MHD-induced Mixing. *Astrophys. J.* **2016**, *818*, 125. [[CrossRef](#)]

21. Nucci, M.C.; Busso, M. Magnetohydrodynamics and Deep Mixing in Evolved Stars. I. Two- and Three-dimensional Analytical Models for the Asymptotic Giant Branch. *Astrophys. J.* **2014**, *787*, 141. [[CrossRef](#)]
22. Vescovi, D.; Cristallo, S.; Busso, M.; Liu, N. Magnetic-buoyancy-induced Mixing in AGB Stars: Presolar SiC Grains. *Astrophys. J. Lett.* **2020**, *897*, L25. [[CrossRef](#)]
23. Nordhaus, J.; Blackman, E.G.; Frank, A. Isolated versus common envelope dynamos in planetary nebula progenitors. *Mon. Not. R. Astron. Soc.* **2007**, *376*, 599–608. [[CrossRef](#)]
24. Kawka, A. The properties and origin of magnetic fields in white dwarfs. *Contrib. Astron. Obs. Skaln. Pleso* **2018**, *48*, 228–235.
25. Battino, U.; Pignatari, M.; Ritter, C.; Herwig, F.; Denisenkov, P.; Den Hartogh, J.W.; Trappitsch, R.; Hirschi, R.; Freytag, B.; Thielemann, F.; et al. Application of a Theory and Simulation-based Convective Boundary Mixing Model for AGB Star Evolution and Nucleosynthesis. *Astrophys. J.* **2016**, *827*, 30. [[CrossRef](#)]
26. Battino, U.; Tattersall, A.; Lederer-Woods, C.; Herwig, F.; Denisenkov, P.; Hirschi, R.; Trappitsch, R.; den Hartogh, J.W.; Pignatari, M.; NuGrid Collaboration. NuGrid stellar data set—III. Updated low-mass AGB models and s-process nucleosynthesis with metallicities $Z = 0.01$, $Z = 0.02$, and $Z = 0.03$. *Mon. Not. R. Astron. Soc.* **2019**, *489*, 1082–1098. [[CrossRef](#)]
27. Adsley, P.; Battino, U.; Best, A.; Cacioli, A.; Guglielmetti, A.; Imbriani, G.; Jayatissa, H.; La Cognata, M.; Lamia, L.; Masha, E.; et al. Reevaluation of the $^{22}\text{Ne}(\alpha, \gamma)^{26}\text{Mg}$ and $^{22}\text{Ne}(\alpha, n)^{25}\text{Mg}$ reaction rates. *Phys. Rev. C* **2021**, *103*, 015805. [[CrossRef](#)]
28. Ota, S.; Christian, G.; Lotay, G.; Catford, W.N.; Bennett, E.A.; Dede, S.; Doherty, D.T.; Hallam, S.; Hooker, J.; Hunt, C.; et al. Decay properties of $^{22}\text{Ne} + \alpha$ resonances and their impact on s-process nucleosynthesis. *Phys. Lett. B* **2020**, *802*, 135256. [[CrossRef](#)]
29. Piersanti, L.; Cristallo, S.; Straniero, O. The Effects of Rotation on s-process Nucleosynthesis in Asymptotic Giant Branch Stars. *Astrophys. J.* **2013**, *774*, 98. [[CrossRef](#)]
30. Liu, N.; Savina, M.R.; Gallino, R.; Davis, A.M.; Bisterzo, S.; Gyngard, F.; Käppeler, F.; Cristallo, S.; Dauphas, N.; Pellin, M.J.; et al. Correlated Strontium and Barium Isotopic Compositions of Acid-cleaned Single Mainstream Silicon Carbides from Murchison. *Astrophys. J.* **2015**, *803*, 12. [[CrossRef](#)]
31. Palmerini, S.; Trippella, O.; Busso, M.; Vescovi, D.; Petrelli, M.; Zucchini, A.; Frondini, F. s-Processing from MHD-induced mixing and isotopic abundances in presolar SiC grains. *Geochim. Cosmochim. Acta* **2018**, *221*, 21–36. [[CrossRef](#)]
32. Liu, N.; Stephan, T.; Cristallo, S.; Gallino, R.; Boehnke, P.; Nittler, L.R.; O'D. Alexander, C.M.; Davis, A.M.; Trappitsch, R.; Pellin, M.J.; et al. Presolar Silicon Carbide Grains of Types Y and Z: Their Molybdenum Isotopic Compositions and Stellar Origins. *Astrophys. J.* **2019**, *881*, 28. [[CrossRef](#)]
33. Herwig, F.; Freytag, B.; Fuchs, T.; Hansen, J.P.; Hueckstaedt, R.M.; Porter, D.H.; Timmes, F.X.; Woodward, P.R. Convective and Non-Convective Mixing in AGB Stars. In *Why Galaxies Care About AGB Stars: Their Importance as Actors and Probes*; Astronomical Society of the Pacific Conference Series; Kerschbaum, F., Charbonnel, C., Wing, R.F., Eds.; Astronomical Society of the Pacific: San Francisco, CA, USA, 2007; Volume 378, p. 43.
34. Werner, K.; Herwig, F. The Elemental Abundances in Bare Planetary Nebula Central Stars and the Shell Burning in AGB Stars. *Publ. Astron. Soc. Pac.* **2006**, *118*, 183–204. [[CrossRef](#)]
35. Zinner, E. Presolar Grains. In *Treatise on Geochemistry*, 2nd ed.; Elsevier: Oxford, UK, 2014; Volume 1, pp. 181–213. [[CrossRef](#)]
36. Pignatari, M.; Herwig, F.; Hirschi, R.; Bennett, M.; Rockefeller, G.; Fryer, C.; Timmes, F.X.; Ritter, C.; Heger, A.; Jones, S.; et al. NuGrid Stellar Data Set. I. Stellar Yields from H to Bi for Stars with Metallicities $Z = 0.02$ and $Z = 0.01$. *Astrophys. J. Suppl. Ser.* **2016**, *225*, 24. [[CrossRef](#)]
37. Paxton, B.; Bildsten, L.; Timmes, F.; Nelson, L.; Lesaffre, P.; Herwig, F.; Dotter, A.; VandenBerg, D.; Sigurson, S.; Hirschi, R.; et al. MESA: Modules for Experiments in Stellar Astrophysics. 2010. Available online: <http://mesa.sourceforge.net> (accessed on 27 July 2020).
38. Grevesse, N.; Noels, A. Cosmic abundances of the elements. In *Origin and Evolution of the Elements*; Prantzos, N., Vangioni-Flam, E., Casse, M., Eds.; Cambridge University Press: Cambridge, UK, 1993; pp. 15–25.
39. Ritter, C.; Andrassy, R.; Côté, B.; Herwig, F.; Woodward, P.R.; Pignatari, M.; Jones, S. Convective-reactive nucleosynthesis of K, Sc, Cl and p-process isotopes in O-C shell mergers. *Mon. Not. R. Astron. Soc.* **2018**, *474*, L1–L6. [[CrossRef](#)]
40. Herwig, F. The evolution of AGB stars with convective overshoot. *Astron. Astrophys.* **2000**, *360*, 952–968.
41. Herwig, F. Evolution of Asymptotic Giant Branch Stars. *Annu. Rev. Astron. Astrophys.* **2005**, *43*, 435–479. [[CrossRef](#)]
42. Arnett, W.D.; Meakin, C.; Viallet, M.; Campbell, S.W.; Lattanzio, J.C.; Mocák, M. Beyond Mixing-length Theory: A Step Toward 321D. *Astrophys. J.* **2015**, *809*, 30. [[CrossRef](#)]
43. Valle, G.; Dell'Omodarme, M.; Prada Moroni, P.G.; Degl'Innocenti, S. Mixing-length calibration from field stars. An investigation on statistical errors, systematic biases, and spurious metallicity trends. *Astron. Astrophys.* **2019**, *623*, A59. [[CrossRef](#)]
44. Vitense, E. Die Wasserstoffkonvektionszone der Sonne. Mit 11 Textabbildungen. *Z. Astrophys.* **1953**, *32*, 135.
45. Böhm, K.H. Über die Größe der Konvektionselemente in Schichten mit variablem Temperaturgradienten. Mit 2 Textabbildungen. *Z. Astrophys.* **1958**, *46*, 245.
46. Tayar, J.; Somers, G.; Pinsonneault, M.H.; Stello, D.; Mints, A.; Johnson, J.A.; Zamora, O.; García-Hernández, D.A.; Maraston, C.; Serenelli, A.; et al. The Correlation between Mixing Length and Metallicity on the Giant Branch: Implications for Ages in the Gaia Era. *Astrophys. J.* **2017**, *840*, 17. [[CrossRef](#)]
47. Pinsonneault, M.H.; Elsworth, Y.; Epstein, C.; Hekker, S.; Mészáros, S.; Chaplin, W.J.; Johnson, J.A.; García, R.A.; Holtzman, J.; Mathur, S.; et al. The APOKASC Catalog: An Asteroseismic and Spectroscopic Joint Survey of Targets in the Kepler Fields. *Astrophys. J. Suppl. Ser.* **2014**, *215*, 19. [[CrossRef](#)]

48. Porter, D.H.; Woodward, P.R. Three-dimensional Simulations of Turbulent Compressible Convection. *Astrophys. J. Suppl. Ser.* **2000**, *127*, 159–187. [[CrossRef](#)]
49. Cseh, B.; Lugaro, M.; D’Orazi, V.; de Castro, D.B.; Pereira, C.B.; Karakas, A.I.; Molnár, L.; Plachy, E.; Szabó, R.; Pignatari, M.; et al. The s process in AGB stars as constrained by a large sample of barium stars. *Astron. Astrophys.* **2018**, *620*, A146. [[CrossRef](#)]
50. Karinkuzhi, D.; Van Eck, S.; Goriely, S.; Siess, L.; Jorissen, A.; Merle, T.; Escorza, A.; Masseron, T. Low-mass low-metallicity AGB stars as an efficient i-process site explaining CEMP-rs stars. *arXiv* **2020**, arXiv:2010.13620.
51. Roederer, I.U.; Lawler, J.E.; Holmbeck, E.M.; Beers, T.C.; Ezzeddine, R.; Frebel, A.; Hansen, T.T.; Ivans, I.I.; Karakas, A.I.; Placco, V.M.; et al. Detection of Pb II in the Ultraviolet Spectra of Three Metal-poor Stars. *Astrophys. J. Lett.* **2020**, *902*, L24. [[CrossRef](#)]
52. Hansen, C.J.; Koch, A.; Mashonkina, L.; Magg, M.; Bergemann, M.; Sitnova, T.; Gallagher, A.J.; Ilyin, I.; Caffau, E.; Zhang, H.W.; et al. Mono-enriched stars and Galactic chemical evolution. Possible biases in observations and theory. *Astron. Astrophys.* **2020**, *643*, A49. [[CrossRef](#)]
53. Mashonkina, L.; Ryabtsev, A.; Frebel, A. Non-LTE effects on the lead and thorium abundance determinations for cool stars. *Astron. Astrophys.* **2012**, *540*, A98. [[CrossRef](#)]
54. Van Aarle, E.; Van Winckel, H.; De Smedt, K.; Kamath, D.; Wood, P.R. Detailed abundance study of four s-process enriched post-AGB stars in the Large Magellanic Cloud. *Astron. Astrophys.* **2013**, *554*, A106. [[CrossRef](#)]
55. De Smedt, K.; Van Winckel, H.; Kamath, D.; Siess, L.; Goriely, S.; Karakas, A.I.; Manick, R. Detailed homogeneous abundance studies of 14 Galactic s-process enriched post-AGB stars: In search of lead (Pb). *Astron. Astrophys.* **2016**, *587*, A6. [[CrossRef](#)]
56. Pereira, C.B.; Drake, N.A. High-resolution spectroscopic observations of two chemically peculiar metal-poor stars: HD 10613 and BD+04 2466. *Astron. Astrophys.* **2009**, *496*, 791–804. [[CrossRef](#)]
57. De Castro, D.B.; Pereira, C.B.; Roig, F.; Jilinski, E.; Drake, N.A.; Chavero, C.; Sales Silva, J.V. Chemical abundances and kinematics of barium stars. *Mon. Not. R. Astron. Soc.* **2016**, *459*, 4299–4324. [[CrossRef](#)]
58. Karinkuzhi, D.; Van Eck, S.; Jorissen, A.; Goriely, S.; Siess, L.; Merle, T.; Escorza, A.; Van der Swaelmen, M.; Boffin, H.M.J.; Masseron, T.; et al. When binaries keep track of recent nucleosynthesis. The Zr-Nb pair in extrinsic stars as an s-process diagnostic. *Astron. Astrophys.* **2018**, *618*, A32. [[CrossRef](#)]
59. Cristallo, S.; Piersanti, L.; Straniero, O.; Gallino, R.; Domínguez, I.; Abia, C.; Di Rico, G.; Quintini, M.; Bisterzo, S. Evolution, Nucleosynthesis, and Yields of Low-mass Asymptotic Giant Branch Stars at Different Metallicities. II. The FRUITY Database. *Astrophys. J. Suppl. Ser.* **2011**, *197*, 17. [[CrossRef](#)]
60. Fishlock, C.K.; Karakas, A.I.; Lugaro, M.; Yong, D. Evolution and Nucleosynthesis of Asymptotic Giant Branch Stellar Models of Low Metallicity. *Astrophys. J.* **2014**, *797*, 44. [[CrossRef](#)]
61. Van Winckel, H.; Reyniers, M. A homogeneous study of the s-process in the 21 μ m carbon-rich post-AGB objects. *Astron. Astrophys.* **2000**, *354*, 135–149.
62. Cristallo, S.; Abia, C.; Straniero, O.; Piersanti, L. On the need of the Light Elements Primary Process (LEPP). *Astrophys. J.* **2015**, *801*, 53. [[CrossRef](#)]